Triplet-State Investigations of Fluorescent Dyes at Dielectric Interfaces Using Total Internal Reflection Fluorescence Correlation Spectroscopy

Hans Blom,*,†,‡ Andriy Chmyrov,†,‡ Kai Hassler,†,§ Lloyd M. Davis,|| and Jerker Widengren*,†

Department of Biomolecular Physics, Royal Institute of Technology, Stockholm, Sweden, and Center for Laser Applications, University of Tennessee Space Institute, Tullahoma, Tennessee 37388

Received: December 13, 2008; Revised Manuscript Received: March 17, 2009

The triplet-state kinetics of several fluorescent dyes used in ultrasensitive fluorescence microscopy are investigated using total internal reflection fluorescence correlation spectroscopy (TIR-FCS). A theoretical outline of the correlation analysis and the physical aspects of evanescent excitation and fluorescence emission at dielectric interfaces are given. From this analysis, the rates of intersystem crossing and triplet decay are deduced for fluorescein, ATTO 488, rhodamine 110, rhodamine 123, and rhodamine 6G in aqueous buffer solutions. All investigated dyes show slightly higher triplet rates at the dielectric interface compared to bulk solution measurements. We attribute this enhancement to possible modifications of the dyes' photophysical properties near a dielectric interface. In the case of rhodamine 6G, the impact of changes in the dye concentration, ionic strength of the solvent, and potassium iodide concentration are also investigated. This leads to a better understanding of the influences of dye−dye, dye−solvent, and dye−surface interactions on the increased triplet intersystem crossing and triplet decay rates. The study shows that analysis of triplet-state kinetics by TIR-FCS not only results in a better understanding of how the photophysical properties of the dyes are affected by the presence of an interface, but also provides a means for probing the microenvironment near dielectric interfaces.

Introduction

Fluorescence microscopy nowadays enables us to directly visualize and track individual biomolecules in their native environment.[1,2] Additionally, new super-resolution techniques even allow biological systems to be studied at the molecular scale[3] and in real time.[4] The exploration of life science by fluorescence microscopy is however challenging because the reporter molecule generating the signal often becomes *exhausted* before revealing the desired scientific answer. The emission rate of a single fluorescent dye molecule is in large determined by the excitation irradiance (i.e., W/cm^2) at which saturation of the excited singlet state is reached, and this in turn depends on the mean occupancy of the triplet state. Additionally, the finite photodegradation of fluorescent molecules sets a limit on the total signal collected from the molecules. For many fluorescent dyes, the rate of irreversible photodegradation is known to be proportional to the triplet-state population.[5–10] It is therefore important to keep this population low to decrease the rate of photodestruction of individual fluorophores.

An often used approach to reduce the triplet-state population in fluorescence-based single-molecule detection is to decrease the excitation irradiance.[11] While this prolongs the period over which fluorescent molecules may be observed, the lower signal makes statistical analysis more difficult and forces longer data acquisition times or additional repetitions of the experiment to be performed. A further possibility is to excite the fluorescent molecules with laser pulses having low enough duty cycle to allow the fluorophores to relax from the triplet state to the singlet ground state before the next excitation can occur.[12–16] Unfortunately, modulated excitation with low repetition rates generally leads to increased measurement times. Fast repetitive scanning of the excitation over the sample could also reduce the photobleaching as this approach gives enough time for the triplet state to decay.[17,18] Another approach to keep the triplet-state population low is to add reducing and oxidizing chemical compounds (so-called triplet quenchers). These compounds decrease the triplet-state population by quenching the triplet state itself (or similar metastable dark states) or through reactions with radicals formed via the triplet state.[19–22] It is also possible to chemically attach to the fluorophore a triplet quencher, which depopulates the triplet state by means of intramolecular energy transfer and hence increases photostability.[23] To achieve additional photochemical stability, oxygen is often removed from the solution.[19,21,24–26] Oxygen is known to react with fluorophores in the triplet state, thereby producing highly reactive singlet oxygen, which may induce damage to the fluorophores as well as to a live cell system.[18] However, removal of oxygen alone leads to severe triplet-state population buildup as oxygen is involved in quenching the triplet state. This then worsens the fluorescence signal as fluorescence emission saturates at a lower rate. To counteract these problems, removal of oxygen and subsequent addition of triplet quenchers can be used.[19,21] Finally, reverse intersystem crossing (ReISC) pumping, an all optical approach, also allows depopulating the triplet state.[27,28] After initial excitation of the fluorophore, a second red-shifted excitation depopulates the lowest triplet state via pumping into higher triplet states and subsequent crossover into the singlet manifold. This results in reduced triplet population and enhanced fluorescence emission. The drawback of the method is that, by populating the higher triplet and singlet states, increased photobleaching may occur.[7,8]

* To whom correspondence should be addressed. Phone: +46-8-55378030. Fax: +46-8-55378216. E-mail: hblom@kth.se (H.B.); jwideng@kth.se (J.W.).
† Royal Institute of Technology.
‡ These authors contributed equally to this work.
§ Present address: SCANCO Medical AG, Limmatstrasse 125, 8005 Zürich, Switzerland.
|| University of Tennessee Space Institute.

10.1021/jp8110088 CCC: $40.75
Published on Web 04/17/2009

As the triplet state plays an important role in the saturation of the fluorescence emission, the finite photodegradation lifetime of the fluorophore, and the production of highly reactive oxygen species, it is important to investigate its kinetics under different experimental conditions. Even though the triplet state is considered to be a major villain with few redeeming virtues,[11] it has actually been possible to take advantage of its properties in optical microscopy to reach beyond the diffraction limit[29–32] or for microenvironmental imaging.[33] Fundamental studies of identifying the existence of the triplet state in fluorophores have been performed since the 1940s.[34–36] In the 1970s, during dye-laser development, much attention was paid to understanding the properties of the triplet state and its influence on laser action.[37,38] Moreover, since the 1990s the extended use of ultrasensitive fluorescence microscopy[39–41] has resulted in a large interest in monitoring triplet-state kinetics. An increased understanding of the triplet-state properties for different fluorophores in matrixes,[42–45] in solution,[46–48] at surfaces,[49,50] and in nanowells[51] has been achieved. The photokinetics of fluorescent molecules can be studied either by autocorrelation analysis of the sequence of fluorescence photons or through statistical analysis of the on- and off-time periods of the fluorescence emission. In the latter method a suitable threshold is needed to define the on- and off-times of the fluorescence emission before statistical analysis of the photodynamics can be performed. In the first method, there is no need to define a threshold as the autocorrelation function is directly accumulated from the measured sequence of photons. Furthermore, for deducing the triplet dynamics of single fluorophores, correlation analysis has been shown to be more reliable, especially at low signal-to-background ratios.[50] However, a potential drawback with correlation analysis is that a correct model of the investigated system is needed to deduce the triplet-state kinetics.

Correlation analysis of the sequence of fluorescence photons, dubbed fluorescence correlation spectroscopy (FCS), was introduced in the 1970s.[52] Two decades later, this technique reached single-molecule sensitivity by using confocal microscopy with high numerical-aperture objectives and single-photon counting avalanche photodiodes as detectors.[53] This helped to establish FCS as a commonly and extensively used tool to attack problems over a wide range of scientific fields.[54] Parallel to the use of confocal microscopy, evanescent excitation for examining dynamical processes at surfaces with FCS has been established.[55] This idea was successfully applied in very early FCS experiments, and in fact, it was the natural way to achieve a small observation volume before the adaption of confocal microscopy. By exciting only a very thin section, typically less than 100 nm thick, one elegantly confines the observation volume along the optical axis. Typically, a reduction factor of 5−10 can be gained compared to a conventional confocal microscope, which provides an observation volume that extends about 1 μm along the optical axis. By the combination of evanescent excitation and confocal microscopy, even smaller observation volumes can be generated, allowing analysis of single fluorophores at higher concentrations.[56–58] The theoretical basis of total internal reflection fluorescence correlation spectroscopy (TIR-FCS) and the first experimental results were already demonstrated by Thompson et al. in the early 1980s.[59,60] Since then, TIR-FCS has been used to investigate processes at interfaces, such as reversible adsorption/desorption kinetics of dye molecules[61,62] and monodisperse polymers[63] to solid surfaces, dye transport in sol−gel films,[64] ligand−receptor kinetics,[65] antibody diffusion near phospholipid bilayers,[66,67] DNA-binding,[68] kinetics of single enzymes,[69] protein and surfactant interactions,[70] and lateral mobility of proteins in cellular membranes.[71] A significant amount of work has also been devoted to deriving accurate theoretical models in TIR-FCS.[60,65,66,72]

In this study we investigate the photokinetics of several fluorescent dyes at dielectric interfaces using total internal reflection fluorescence correlation spectroscopy. To our knowledge, this is the first study that rigorously investigates triplet-state kinetics at interfaces using TIR-FCS. The study starts with a theoretical outline of correlation analysis and photophysical aspects of evanescent excitation and fluorescence emission at dielectric interfaces. From this analysis, the rates of intersystem crossing and triplet decay are deduced for fluorescein, ATTO 488, rhodamine 110, rhodamine 123, and rhodamine 6G.

Experimental Methods

To deduce the triplet rates at interfaces, we follow the approach introduced by Widengren et al. for bulk solution studies using confocal FCS.[46,47] Modifications of the theory to account for the properties of excitation by total internal reflection and nonisotropic emission from a molecule near a surface have been introduced accordingly. This is presented in the following section, together with the correlation analysis approach and the electronic-state rate equations used to deduce the triplet-state kinetics.

Evanescent Excitation. The physical aspects of evanescent excitation using TIR have been described previously.[73,74] When a laser beam propagates through a high refractive index material (glass, $n_1 = 1.52$) and encounters a low refractive index material (water, $n_2 = 1.33$), usually a portion is reflected and most is transmitted while being refracted toward the interface. For total reflection to occur, the sine of the angle of incidence (measured from the normal of the interface) must exceed the ratio of the refractive indices of the interfacing media, i.e., $\theta > \sin^{-1}(n_2/n_1) \approx 61°$. At and above this critical angle, the propagating beam is totally back-reflected from the interface. Within the low index material there is a nonpropagating evanescent field, which is in general elliptically polarized. The irradiance that will be experienced by an absorbing molecule in the evanescent field decays exponentially with distance z from the surface:

$$I(z) = I(0)\exp(-z/d) \tag{1}$$

The characteristic decay length at which the irradiance decays by a factor of $1/e$ is given by the penetration depth, $d = \lambda_0/4\pi(n_1^2 \sin^2\theta - n_2^2)^{-1/2}$, where λ_0 is the excitation wavelength in a vacuum. However, the level of irradiance that would be seen by a molecule at the surface, $I(0)$, may be greater than the irradiance that would be produced by the incident laser beam in free space, I_0. This is evident in the equations that give the evanescent field irradiance contributions from parallel (P-pol) and perpendicularly (S-pol) polarized incident light, I_0^P and I_0^S, as a function of the angle of incidence:[73,74]

$$I^P(0) = I_0^P \frac{(4\cos^2\theta)(2\sin^2\theta - n^2)}{n^4\cos^2\theta + \sin^2\theta - n^2} \tag{2a}$$

$$I^S(0) = I_0^S \frac{4\cos^2\theta}{1 - n^2} \tag{2b}$$

where $n = n_2/n_1$. Up to a factor of 5 in enhancement of the excitation intensity is possible using TIR excitation on a glass/water interface. This enhancement factor can be increased even further on metal films.[73,74] The maximum enhancement is reached when the beam incident is at the critical angle and the axial extent of the evanescent field approaches very large values. Figure 1 shows the resulting levels of irradiance due to the

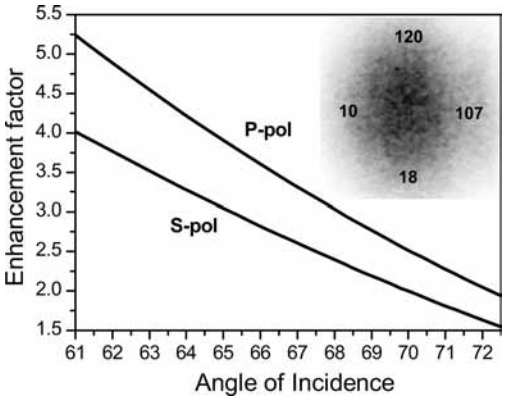

Figure 1. Normalized enhancement factor of the evanescent field at a glass ($n_2 = 1.33$) and water ($n_1 = 1.52$) interface for P-pol and S-pol incident light as a function of the angle of incidence (AOI). For normalization, the incident intensities are set equal to unity ($I_0^P = I_0^S = 1$) in eqs 2a and 2b. Inset: Detected lateral fluorescence intensity distribution on the iXon EMCCD camera including the $1/e^2$ pixel values (24 μm pixel size, total magnification 122 times).

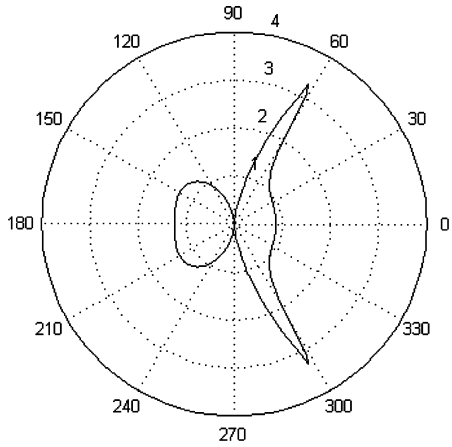

Figure 2. Normalized radiated power displayed as a polar plot assuming a randomly oriented dipole located at the water/glass interface, $z = 0$. The right half ($\pm 90°$) shows the highly anisotropic emission into the glass, with a maximum around the critical angle ($\theta_c \approx \pm 61°$), which can be collected by the high numerical-aperture microscope objective. The normalization is such that radiated power is scaled to that of the same dipole in the absence of the interface (which has a value of 1 on this graph).

evanescent field for different angles of incidence for P- and S-polarized incident light. The enhancement η for circularly polarized incident light is given by the mean of the values for P and S polarization:

$$\eta = \frac{I(0)}{I_0} = \left(\frac{(4\cos^2\theta)(2\sin^2\theta - n^2)}{n^4\cos^2\theta + \sin^2\theta - n^2} + \frac{4\cos^2\theta}{1-n^2} \right)/2 \quad (3)$$

To allow a correct estimate of the triplet rates, this enhancement in excitation irradiance is incorporated into the following analysis.

Nonisotropic Emission. It has long been known that fluorescence emission from dye molecules located near an interface of two media with different refractive indices (glass/water) is highly anisotropic.[75–77] The discontinuity in the refractive index produces a significant modification of the angular dependence of emitted power, which has a maximum of fluorescence emission in the direction of the critical angle.[78,79] Figure 2 shows the emission profile from a randomly oriented fluorophore located right at the glass/water interface. The radiation pattern was calculated in Matlab using the simple input−output formalism introduced by Mertz.[80] As can be seen, much of the emission is directed toward the glass side at an angle greater than or equal to the critical angle ($\theta_c \approx 61°$). This supercritical emission also results in an increase of the fluorescence emission rate as compared to isotropic emission generated without an interface.

When deriving an estimate of the detected fluorescence emission rate in TIR-FCS, not only the characteristic of evanescent excitation, but also the anisotropic emission and its optical collected have to be considered. The detected fluorescence, $F(\mathbf{r},t)$, depends on the collection efficiency function of the microscope, CEF($\mathbf{r}$), the concentration of the fluorophore, $C(\mathbf{r},t)$, and the emission rate of the fluorophore located at a position $\mathbf{r}$. The emission rate is proportional to the probability for the fluorophore to be in the first excited singlet state, $S_1(\mathbf{r},t)$, its fluorescence quantum yield, ϕ_f, and the inverse of the fluorescence lifetime, τ_f^{-1}. The fluorescence rate per unit volume detected from a point $\mathbf{r}$ at time t may then be expressed as

$$F(\mathbf{r},t) = q[\mathrm{CEF}(\mathbf{r})]\phi_f\tau_f^{-1}S_1(\mathbf{r},t)\,N_A C(\mathbf{r},t) \quad (4)$$

where q accounts for the detection quantum yield of the microscope and N_A is Avogadro's number. Any fluorescence fluctuations detected from the observation volume are governed by the two stochastic variables, $S_1(\mathbf{r},t)$ and $C(\mathbf{r},t)$, which are independent and which have fluctuations that occur on different time scales. Fluctuations will be caused either by variation in the population statistics of the first excited singlet state due to singlet−triplet transitions or by diffusion of fluorophores in and out of the observation volume. Diffusion of nanometer-sized particles has been shown to slow and becomes nonlinear when within less than 1 μm of an interface.[81] In this work we assume that the diffusion is ideal so that the variance of the concentration is equal to the steady-state fluorophore concentration $\bar{C}(\mathbf{r})$. Furthermore, the time resolution of our experiment only allows us to observe the steady-state value of the first excited singlet state, $\bar{S}_1(\mathbf{r})$, which is the first term of eq 2A in the Appendix. This means that any changes seen in the emission probability, as governed by $\bar{S}_1(\mathbf{r})$, instantaneously adapt to changes in the occupancy of the triplet state.

Additionally, the dependence of the detected fluorescence on the distance from the surface is taken into account by introducing the function $H(z)$, the fraction of power emitted by a single fluorophore at a distance z from the interface into the cone of light accepted by the microscope objective, relative to the fraction from a fluorophore without the interface (i.e., relative to that for $z \to \infty$).[82,83] The collection efficiency function in eq 4 is hence calculated according to the following convolution:

$$\mathrm{CEF}(\mathbf{r}) = H(z)\int_S \mathrm{circ}(\rho'/a)\,\mathrm{PSF}(\rho'-\rho, z)\,\mathrm{d}\rho' \quad (5)$$

where PSF denotes the usual point spread function of the microscope, i.e., the intensity distribution produced in image space ρ' from a single fluorophore located at position $\mathbf{r} = (\rho,z)$ in object space. The transmission function of the pinhole is represented by the circ function, which is unity for arguments smaller than the projected pinhole size, a, which is defined as the pinhole size divided by the magnification of the microscope.[84]

Correlation Analysis. By use of FCS, it is in principle possible to deduce information about any dynamical process that manifests itself as a change in fluorescence intensity.[54] To obtain this information, the fluorescence photon counts are analyzed in terms of an autocorrelation function, $G(\tau)$, which can be defined as $G(\tau) = \langle F(t)\,F(t+\tau)\rangle/\langle F\rangle^2 - 1$, where the

angular brackets denote averaging over time, t. Insertion of eq 4 with $\bar{S}_1(\mathbf{r},t)$ determined by the evanescent excitation irradiance (see the following section), and replacement of the time averaging with spatial averaging over the observation volume, generates the following autocorrelation function:[83]

$$G(\tau) = \frac{\gamma}{N}\left\{1 + \frac{\bar{T}}{1-\bar{T}}\exp\left(-\frac{\tau}{\bar{\tau}_t}\right)\right\} \left[\left(1 - \frac{\tau}{2\tau_z}\right)w\left(i\sqrt{\frac{\tau}{4\tau_z}}\right) + \sqrt{\frac{4\tau}{\pi\tau_z}}\right]\left(1 + s^2\frac{\tau}{\tau_z}\right)^{-1} \quad (6)$$

In this equation, which describes triplet-state kinetics and free diffusion within an evanescent excitation field, N is the mean number of molecules within the observation volume, $\bar{T}$ is the spatially averaged steady-state probability of the molecules to be in the triplet state, and $\bar{\tau}_t$ denotes the spatially averaged steady-state triplet relaxation time. The average axial diffusion time is defined as $\tau_z = h^2/4D$, where D is the diffusion coefficient and h is the axial extent of the observation volume, which is approximately equal to d, the penetration depth of the evanescent field. The function w is the complex generalization of the error function defined as $w(x) \equiv \exp(-x^2)\,\mathrm{erfc}(-ix)$. The parameter γ describes a geometrical correction factor of the observation volume, and its value was derived through evaluation of the observation volume by numerical calculations.[83] The parameter $s = h/b$ describes a scaling factor, with b being the radius of the observation volume in the lateral direction ($1/e^2$ value). To fit the TIR-FCS data, a multidimensional least-squares algorithm written in Matlab (Mathworks Inc.) was used to estimate the unknown parameters of eq 6, N, $\bar{T}$, $\bar{\tau}_t$, and τ_z.

Electronic-State Model. The electronic states of fluorescent dye molecules can, in many cases, be approximated with a simple three-level system as shown in Figure 9 in the Appendix. Here, S_0 denotes the singlet ground state, S_1 is the first excited singlet state, and T is the first excited triplet state. Transition rates between the electronic states are given by k_{01}, k_{10}, k_{ISC}, and k_T, which denote the excitation rate, the fluorescence rate, the intersystem crossing rate, and the decay rate of the triplet state. The applied electronic-state model is highly suitable for our TIR-FCS investigations, as the irradiances are low to moderate (i.e., <50 kW/cm^2). Only for higher irradiances (>100 kW/cm^2), a five-level system is more applicable.[7,8,20] Objective-based TIR excitation generates an irradiance that is approximately Gaussian in the lateral direction and exponential in the axial direction:[83]

$$I(\mathbf{r}) = \eta\frac{2P}{\pi R^2}\exp(-2\rho^2/R^2)\exp(-z/d) \quad (7)$$

where η is the TIR enhancement factor given above, P is the incident laser power, and R is the radius of the laser beam at the interface. Note that $R \gg b$, where b is the lateral size of the observation volume defined by the pinhole, and hence, the irradiance within the observation volume is effectively constant in the lateral dimension and hence is given by eq 1 with $I(0) = \eta 2P/\pi R^2$.

The probability of occupying the different electronic states in Figure 9 can be found for different values of $I(\mathbf{r})$ by solving the coupled first-order differential equations of the three-level system (see the Appendix for derivation), wherein the simplifying assumption is made that the singlet−triplet transition is much faster than the diffusion time; i.e., molecules are essentially immobile at different parts of the beam, with different levels of illumination and hence different steady-state triplet kinetics. The steady-state probability at a specific point $\mathbf{r}$ is thus given by the first term in eq 3A in the Appendix. This means that the mean triplet population, T, and the triplet relaxation time τ_t, are given by[46,47]

$$T(\mathbf{r}) = \frac{\sigma I(\mathbf{r})k_{ISC}}{\sigma I(\mathbf{r})(k_{ISC}+k_T) + \tau_f^{-1}k_T} \quad (8a)$$

$$\tau_t(\mathbf{r}) = \left(k_T + \frac{\sigma I(\mathbf{r})k_{ISC}}{\sigma I(\mathbf{r}) + \tau_f^{-1}}\right)^{-1} \quad (8b)$$

As the excitation irradiance is known, the intersystem crossing rate and the triplet relaxation rate in eqs 8a and 8b can be estimated. However, when deriving a correct estimate of the triplet parameters at an interface using experimental measurements by TIR-FCS, it is necessary to weight eqs 8a and 8b to account for the nonuniform detection of the anisotropic fluorescence emission. Hence, to connect the $\bar{T}$ and $\bar{\tau}_t$ values measured by TIR-FCS, with $T(\mathbf{r})$ and $\tau_t(\mathbf{r})$, the latter are actually weighted by the detected fluorescence intensity squared and spatially averaged over the observation volume (see ref 47 for the complete mathematical expressions).

Experimental Setups. The experimental TIR-FCS setup uses a single-line 491 nm diode laser (Calypso, Cobolt AB), the power of which is directly remote controlled by a program written in LabView, and an additional variable neutral density filter (NDC-25C-4, Thorlabs Inc.). The laser beam is made circularly polarized by using a $\lambda/4$ wave plate (Optosigma). An achromatic lens with a focal length of 200 mm focuses the 3.5-fold expanded laser beam at the back-focal plane of an oil immersion objective (α-Plan-Fluar, 100×, NA 1.45, Carl Zeiss). The laser beam is reflected into the objective using a dichroic mirror (F500-Di01, Semrock Inc.). A beam offset of 2.2 mm from the optical axis results in evanescent field excitation, with a lateral diameter at the glass/water interface of about 20 μm ($1/e^2$ value), as measured by an electron- multiplying CCD camera (iXon DU-860, Andor Technology). About 65% of the laser power was delivered to the interface as measured by a power meter (LaserMate, Coherent Inc.). The focusing lens and the dichroic mirror are moved in one block by a linear translator with micrometer screws to adjust the lateral position of the laser beam entering the objective. In this way, the excitation angle can be adjusted without altering the optical path length between the focusing lens and the objective.[69] During measurements, the angle is fixed to a value slightly below 64° (estimated as 63.7°). The emitted fluorescence is collected with the same high-NA objective and focused with an achromatic tube lens onto the central fiber cores of two 50 μm multimode fibers (Fibertech, Berlin, Germany), which are connected to two avalanche photodiodes (SPCM-AQR-14-FC, Perkin-Elmer Optoelectronics). A 50/50 beamsplitter plate (G344143000, Linos) is used to split the fluorescence between the detectors. Band-pass filters (HQ 550/80, Chroma Tech. Corp.) are placed in front of the fibers to block back-reflected and scattered laser light. The detector signals are cross-correlated online using an ALV-6000 correlator (ALV Erlangen, Germany) having a 12.5 ns time resolution.

A spectrofluorometer equipped with a pulsed nanolight-emitting diode at 495 nm (Fluormax-3 TCSPC, Horiba Jobin Yvon) is used to measure the fluorescence relaxation rates of the different fluorophores by time-correlated single-photon counting.[85] A dilute solution of 1% colloidal Ludox beads (Sigma-Aldrich) is used to measure the instrument response function (IRF). All measured decay functions are fitted to a single exponential using the commercial program delivered with the spectrofluorometer (DAS6). To determine the cross sections

at 491 nm, a spectrophotometer (Biochrom 4060 UV/vis, Pharmacia LKB Biochrom, Cambridge, U.K.) is used in absorbance mode. The measured extinction coefficient, ε, is used with the Beer−Lambert equation used to calculate the cross sections, $\sigma = (3.82 \times 10^{-21})\varepsilon$.[86] A 10 mm precision cuvette from Hellma (104.002F-OS) is used in all measurements.

Surface Preparation. The surface preparation of cleaned glass microscope coverslips (no. 1, ∅ = 25 mm, Hecht-Assistent, Germany) is done according to the following protocol: cleaning for 20 min in an ultrasonic bath in a solution of 2% Hellmanex II (Hellma, Germany) and thereafter thorough rinsing in ultrapure water from a Barnstead EASY pure purification system, ultrasonic cleaning for 20 min in an acetone/ethanol mixture (30%/70% by volume) and thorough rinsing, ultrasonic cleaning for 20 min in water and rinsing with water and spectroscopically pure ethanol. The cover glasses are blown dry with nitrogen and oxygen plasma etched for 2 min in a reactive ion etcher (PlasmaLab 80 Plus, Oxford Instrument, United Kingdom). The cleaned cover glasses are then used directly or stored in ultrapure water. The cover glasses are rinsed with ultrapure water and blown dry with nitrogen prior to measurement. An elastic Teflon ring with ∅ = 8 mm is placed on top of the clean hydrophilic cover glasses to prevent the samples from spreading into a thin film. This configuration generates a sample reservoir in the form of a standing droplet, which in addition prevents fast evaporation.

Fluorophores. Fluorescein, rhodamine 110 (Rh110), and rhodamine 123 (Rh123) were purchased from Molecular Probes, and rhodamine 6G perchlorate (Rh6G) and ATTO 488 were purchased from Atto-Tec GmBH. Stock solutions of the different dyes are prepared in spectroscopically pure ethanol or dimethyl sulfoxide (DMSO), and these are diluted in ultrapure water to nanomolar concentrations prior to measurements. Samples are mixed prior to pipetting them onto the clean silica surfaces. The buffers used throughout the TIR-FCS experiments are Tris (pH 8.2 with 150 mM NaCl) for fluorescein and PBS (pH 7.4) for all other dyes. Diluted solutions of potassium iodide (100 mM stock solutions prepared in ultrapure water) are used together with rhodamine 6G. All buffer salts are of analytical grade. The fluorescence quantum yields of all investigated dyes are taken from the literature.

Computer Simulations. Computer simulations of how the concentration of rhodamine 6G molecules in the sample volume is depleted in the presence of bleaching are done using the commercial multiphysics finite element analysis software package from COMSOL. In this software, the dye concentration is calculated by solving the diffusion equation $\partial C(\mathbf{r},t)/\partial t = D\nabla^2 C(\mathbf{r},t) - k_d C(\mathbf{r},t)$ with a negative source term, $k_d C(\mathbf{r},t)$, arising from photodegradation. It is further assumed that the photodegradation rate is proportional to the sum of the steady-state populations of the triplet state and the first excited singlet state, i.e., $k_d = \tau_f^{-1}\Phi_b(\bar{S}_1(\mathbf{r}) + \bar{T}(\mathbf{r}))$. In the simulations, the photodestruction yield per excitation cycle is set to $\Phi_b = 2.5 \times 10^6$ and the rhodamine 6G diffusion coefficient is set to $D = 2.8 \times 10^{-6}$ cm^2 s^{-1}. The steady-state populations, $\bar{S}_1(\mathbf{r})$ and $\bar{T}(\mathbf{r})$, are given as stated before by the first terms of eqs 2A and 3A in the Appendix. To calculate the electronic-state populations, the k_{ISC} and k_T rates are taken for 0 mM potassium iodide concentration measured with confocal FCS. At the higher 2 and 5 mM concentrations, the measured TIR-FCS rates are used. All these rates, together with the inverse of the measured fluorescence lifetimes, are listed in Table 2.

TABLE 1: Obtained Values of the Intersystem Crossing Rates, k_{ISC}, and the Triplet Relaxation Rates, k_T, for Fluorescein (in Tris Buffer, pH 8.2, 150 mM NaCl) and ATTO 488, Rhodamine 110, and Rhodamine 123 (in PBS Buffer, pH 7.4)

	TIR-FCS		confocal FCS	
	k_{ISC} (μs^{-1})	k_T (μs^{-1})	k_{ISC} (μs^{-1})	k_T (μs^{-1})
fluorescein	13.5 ± 1.0	0.66 ± 0.04	11.1 ± 1.0	0.54 ± 0.04
ATTO 488	1.7 ± 0.1	0.32 ± 0.01	1.5 ± 0.1	0.25 ± 0.03
Rh110	1.3 ± 0.1	0.49 ± 0.03	1.0 ± 0.1	0.45 ± 0.04
Rh123	1.2 ± 0.1	0.58 ± 0.04	1.0 ± 0.1	0.53 ± 0.04

Results

To determine the rate constants for intersystem crossing, k_{ISC}, and the decay of the triplet state, k_T, the TIR-FCS autocorrelation function is collected at different excitation intensities. The data are numerically fitted with the correlation function given by eq 6 to extract the experimental values of $\bar{T}$ and $\bar{\tau}_t$. By plotting the experimentally determined $\bar{T}$ and $\bar{\tau}_t$ values as a function of excitation irradiances and simultaneously making nonlinear least-squares fits to the expressions of eqs 8a and 8b, the unknown k_{ISC} and k_T rates are determined. (In the results given for the triplet-state rate analysis, the excitation irradiance is divided by the photon energy for the excitation wavelength of 491 nm, and the result is expressed in units of photons μs^{-1} cm^{-2}.)

Fluorescein. In the upper part of Figure 3 the resulting TIR-FCS autocorrelation functions for fluorescein measured at three different excitation intensities are shown. The measurements

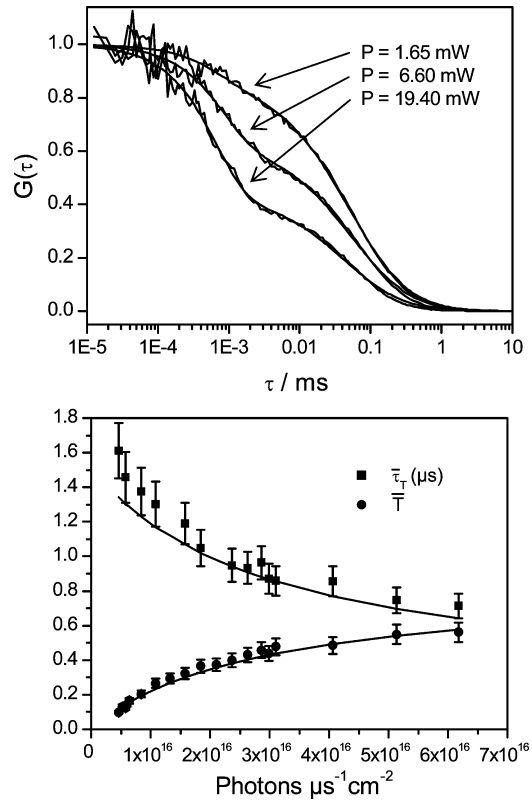

Figure 3. Top: Normalized correlation curves of fluorescein in Tris buffer (pH 8.2 and 150 mM NaCl) at three different laser excitation powers and the corresponding TIR-FCS fits using eq 6. Bottom: Measured triplet-state parameters, $\bar{\tau}_t$ (filled squares) and $\bar{T}$ (filled circles). Error bars show estimated errors of ±10%. Solid lines show the weighted and spatially averaged fits of eqs 8a and 8b, which generated $k_{ISC} = 13.5 \pm 1.0\ \mu s^{-1}$ and $k_T = 0.66 \pm 0.04\ \mu s^{-1}$.

TABLE 2: Obtained Values of the Intersystem Crossing Rates, k_{ISC}, and the Triplet Relaxation Rate, k_T, for Rhodamine 6G with and without Potassium Iodide

	TIR-FCS		confocal FCS[46]	
[KI] (mM)/τ_f^{-1} (μs^{-1})	k_{ISC} (μs^{-1})	k_T (μs^{-1})	k_{ISC} (μs^{-1})	k_T (μs^{-1})
5/284	24.4 ± 1.5	0.71 ± 0.04	28 ± 20%	0.73 ± 10%
2/267	10.8 ± 0.7	0.66 ± 0.03	15 ± 20%	0.61 ± 10%
0.5/257	3.5 ± 0.3	0.72 ± 0.04	5 ± 20%	0.53 ± 10%
0.2/254	1.6 ± 0.1	0.92 ± 0.06	1.6 ± 20%	0.50 ± 10%
0/253	1.6 ± 0.2	1.2 ± 0.1	1.1 ± 20%	0.49 ± 10%

show contributions from triplet-state kinetics and free diffusion. To highlight the kinetics of the triplet state, $G(\tau)$ has been normalized to one at short lag times, τ. This makes it clearly visible that $\bar{T}$ increases and $\bar{\tau}_t$ decreases with increasing excitation intensities, as expected from the electronic-state model of Figure 9. The resulting curves of the extracted values of $\bar{T}$ and $\bar{\tau}_t$ at all measured excitation intensities are displayed in the lower part of Figure 3, together with the corresponding global fits to determine the unknown rates of k_{ISC} and k_T. The extracted values for fluorescein are $k_{ISC} = 13.5 \pm 1.0\ \mu s^{-1}$ and $k_T = 0.66 \pm 0.04\ \mu s^{-1}$, as estimated by using the fluorescence decay rate, $\tau_f^{-1} = 250\ \mu s^{-1}$, and the excitation cross-section, $\sigma = 3.0 \times 10^{-16}$ cm^2, as measured with the spectroflourometer and spectrophotometer.

To be able to compare the intersystem crossing and triplet decay rates deduced by TIR-FCS, with and without the glass surfaces, we also performed FCS measurements of the same sample with a confocal setup, using the original approach introduced by Widengren et al.[47] The analysis of the triplet-state kinetics using confocal FCS gives $k_{ISC} = 11.1 \pm 1.0\ \mu s^{-1}$ and $k_T = 0.54 \pm 0.04\ \mu s^{-1}$, which are similar to the rates measured by TIR-FCS (cf. Table 1). The excitation intensity distribution of the confocal setup is approximated with a Gaussian−Lorentzian function. Slightly lower rates are generated if one assumes a uniform excitation intensity distribution.[46]

ATTO 488, Rhodamine 110, and Rhodamine 123. Figure 4 shows the triplet-state rate analysis of ATTO 488 (top), rhodamine 110 (middle), and rhodamine 123 (bottom) at all measured excitation irradiances. The measured TIR-FCS values of $\bar{T}$ and $\bar{\tau}_t$, together with the global fits to extract k_{ISC} and k_T, for all three dyes are shown. The extracted values for ATTO 488 are $k_{ISC} = 1.7 \pm 0.1\ \mu s^{-1}$ and $k_T = 0.32 \pm 0.01\ \mu s^{-1}$, obtained with the measured values of $\tau_f^{-1} = 312.5\ \mu s^{-1}$ and $\sigma = 2.6 \times 10^{-16}$ cm^2. The intersystem crossing rate and triplet decay rate for rhodamine 110 are $k_{ISC} = 1.3 \pm 0.1\ \mu s^{-1}$ and $k_T = 0.49 \pm 0.03\ \mu s^{-1}$, which are deduced using the measured values of $\tau_f^{-1} = 244\ \mu s^{-1}$ and $\sigma = 2.5 \times 10^{-16}$ cm^2. Finally, the rates for rhodamine 123 are $k_{ISC} = 1.2 \pm 0.1\ \mu s^{-1}$ and $k_T = 0.58 \pm 0.04\ \mu s^{-1}$, deduced with $\tau_f^{-1} = 250\ \mu s^{-1}$ and $\sigma = 2.7 \times 10^{-16}$ cm^2. Table 1 summarizes the deduced TIR-FCS and confocal FCS triplet rates for ATTO 488, rhodamine 110, rhodamine 123, and fluorescein. Confocal FCS gave the following rates: ATTO 488, $k_{ISC} = 1.5 \pm 0.1\ \mu s^{-1}$ and $k_T = 0.25 \pm 0.04\ \mu s^{-1}$; rhodamine 110, $k_{ISC} = 1.0 \pm 0.1\ \mu s^{-1}$ and $k_T = 0.45 \pm 0.04\ \mu s^{-1}$; rhodamine 123, $k_{ISC} = 1.0 \pm 0.1\ \mu s^{-1}$ and $k_T = 0.53 \pm 0.04\ \mu s^{-1}$. The same fluorescence lifetimes and excitation cross sections as used for TIR-FCS are applied in the analysis of confocal FCS measurements.

Rhodamine 6G. Figure 5 shows the triplet-state rate analysis of rhodamine 6G in PBS buffer. The upper graph visualizes the TIR-FCS-measured $\bar{\tau}_t$ and compares this to simulated confocal FCS values. The confocal bulk solution values are calculated by applying eqs 8a and 8b with the assumption of a uniform intensity distribution with the same magnitude as the evanescent field at $z = 0$. The fluorescence decay rate, τ_f^{-1}, and excitation cross section, σ, are assumed to be the same as for TIR-FCS. Additionally, the measured confocal triplet rates $k_{ISC} = 1.1 \pm 0.2\ \mu s^{-1}$ and $k_T = 0.49 \pm 0.05\ \mu s^{-1}$ are applied in the calculation. As can be seen, the triplet decay times of Rh6G at the silica interface are roughly 1 μs faster than those in solution. This is a clear indication that Rh6G molecules in the vicinity of the interface show triplet-state properties different from those of the same chemical species in bulk solution. The middle graph compares the same thing for $\bar{T}$, which shows both lower and higher amplitudes compared to the simulated confocal FCS values. The results again indicate an interface-induced effect which influences the triplet-state kinetics of rhodamine 6G. Evaluation of the TIR-FCS triplet rates is shown in the lower graph in Figure 5, where the corresponding weighted and spatially averaged fitting of the data is done. The fits give k_{ISC}

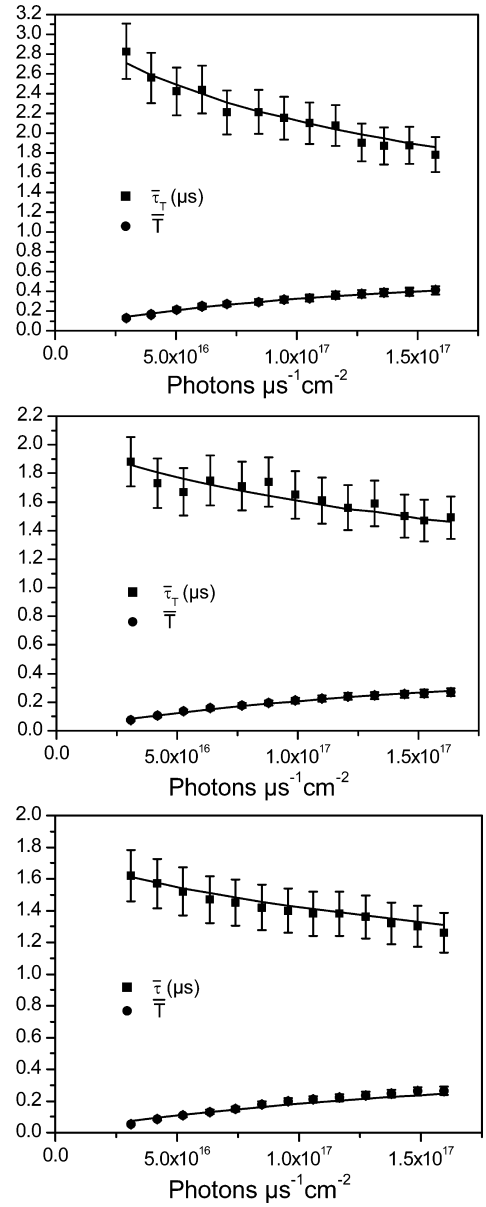

Figure 4. Measured triplet-state parameters, $\bar{\tau}_t$ (filled squares) and $\bar{T}$ (filled circles), and the corresponding weighted and spatially averaged global fits for ATTO 488 (top), $k_{ISC} = 1.7 \pm 0.1\ \mu s^{-1}$ and $k_T = 0.32 \pm 0.01\ \mu s^{-1}$, rhodamine 110 (middle), $k_{ISC} = 1.3 \pm 0.1\ \mu s^{-1}$ and $k_T = 0.49 \pm 0.03\ \mu s^{-1}$, and rhodamine 123 (bottom), $k_{ISC} = 1.2 \pm 0.1\ \mu s^{-1}$ and $k_T = 0.58 \pm 0.04\ \mu s^{-1}$. Error bars show estimated errors of ±10%.

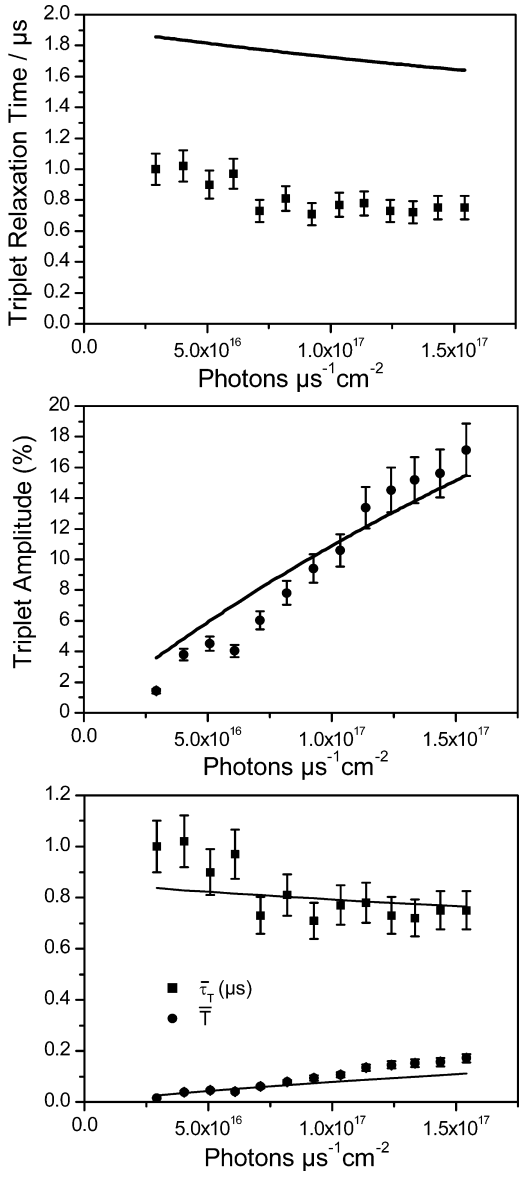

Figure 5. Measured triplet-state parameters for rhodamine 6G, $\bar{\tau}_t$ (filled squares) and $\bar{T}$ (filled circles). Error bars show estimated errors of ±10%. The measured TIR-FCS data points in the upper and middle graphs are compared to simulated confocal FCS values of $\bar{\tau}_t$ and $\bar{T}$, which are shown as solid lines. The lower graph shows the corresponding weighted and spatially averaged global fits of the TIR-FCS data, which give $k_{ISC} = 1.6 \pm 0.2\ \mu s^{-1}$ and $k_T = 1.2 \pm 0.1\ \mu s^{-1}$. The concentration of Rh6G in PBS was 50 nM.

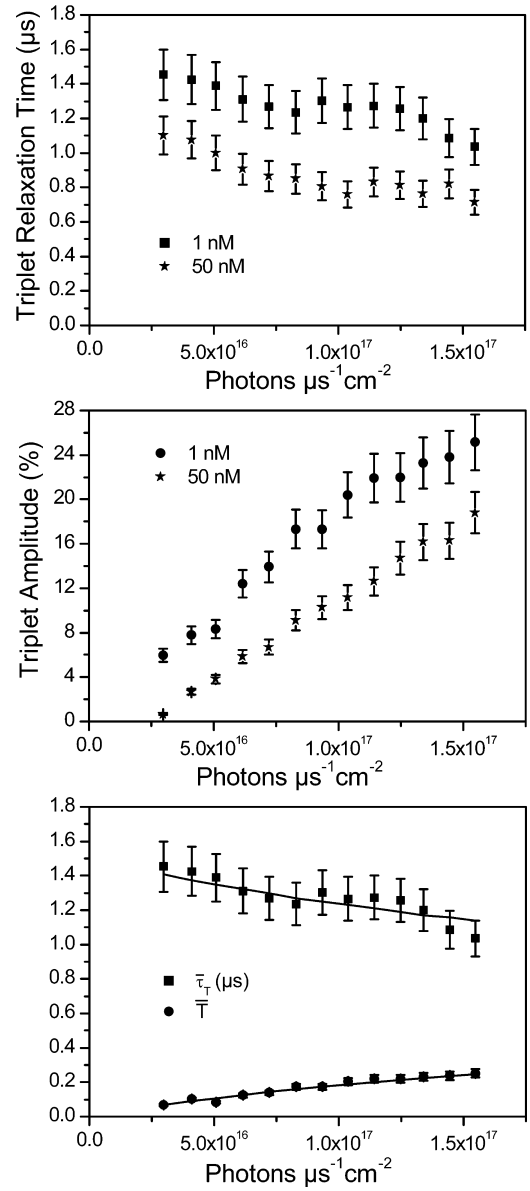

Figure 6. Comparison of measured triplet-state parameters for Rh6G in PBS at two different concentrations (1 and 50 nM). Error bars show estimated errors of ±10%. The upper graph shows $\bar{\tau}_t$ at 1 nM (filled squares) and 50 nM (filled stars). The middle graph shows $\bar{T}$ at 1 nM (filled circles) and 50 nM (filled stars). The lower graph shows the corresponding weighted and spatially averaged global fits of the TIR-FCS data for Rh6G at 1 nM, $k_{ISC} = 2.4 \pm 0.2\ \mu s^{-1}$ and $k_T = 0.66 \pm 0.07\ \mu s^{-1}$, with $\bar{\tau}_t$ (filled squares) and $\bar{T}$ (filled circles).

$= 1.6 \pm 0.2\ \mu s^{-1}$ and $k_T = 1.2 \pm 0.1\ \mu s^{-1}$, which deviate significantly from the confocal FCS rates. Such differences are not seen with the other fluorescent dyes investigated in this work.

To investigate this further, we decided to change the concentration of the Rh6G sample. Figure 6 shows a comparison of the TIR-FCS triplet-state rate analysis of $\bar{\tau}_t$ and $\bar{T}$ at sample concentrations of 1 and 50 nM in PBS. As is clearly visible, a lower concentration generates longer triplet relaxation times and higher triplet amplitudes. The corresponding weighted and spatially averaged fits give $k_{ISC} = 2.4 \pm 0.2\ \mu s^{-1}$ and $k_T = 0.66 \pm 0.07\ \mu s^{-1}$ for the 1 nM solution. After studying the impact of the dye concentration, we also changed the ionic strength of the solvent. Figure 7 shows the measured values of $\bar{\tau}_t$ and $\bar{T}$ for the 1 and 100 mM sodium chloride samples with a rhodamine 6G concentration of 50 nM. An increase of the triplet relaxation times and the triplet amplitude is seen for the lower ionic strength. Evaluation of the 1 mM sodium chloride samples yields $k_{ISC} = 2.1 \pm 0.2\ \mu s^{-1}$ and $k_T = 0.70 \pm 0.05\ \mu s^{-1}$, whereas the higher ionic strength gives rates similar to those of Rh6G in PBS (cf. Figure 5). Having studied the influences of dye−dye and dye−solvent interactions, through the impact of the dye concentration and ionic strength, we finally turned our interest to another dye−solvent effect. Potassium iodide has a strong influence on the triplet-state rate parameters of Rh6G, as already shown with confocal FCS.[14,47] We decided to study this solvent effect also near glass surfaces using TIR-FCS. Figure 8 shows the measured $\bar{\tau}_t$ and $\bar{T}$ values, including weighted and spatially averaged global fits of 50 nM Rh6G in PBS without and with addition of 5 mM potassium iodide. In the correlation curves, a strong buildup of the triplet-state population as well as a reduced triplet relaxation time is seen when potassium iodide is added. The following triplet rates are

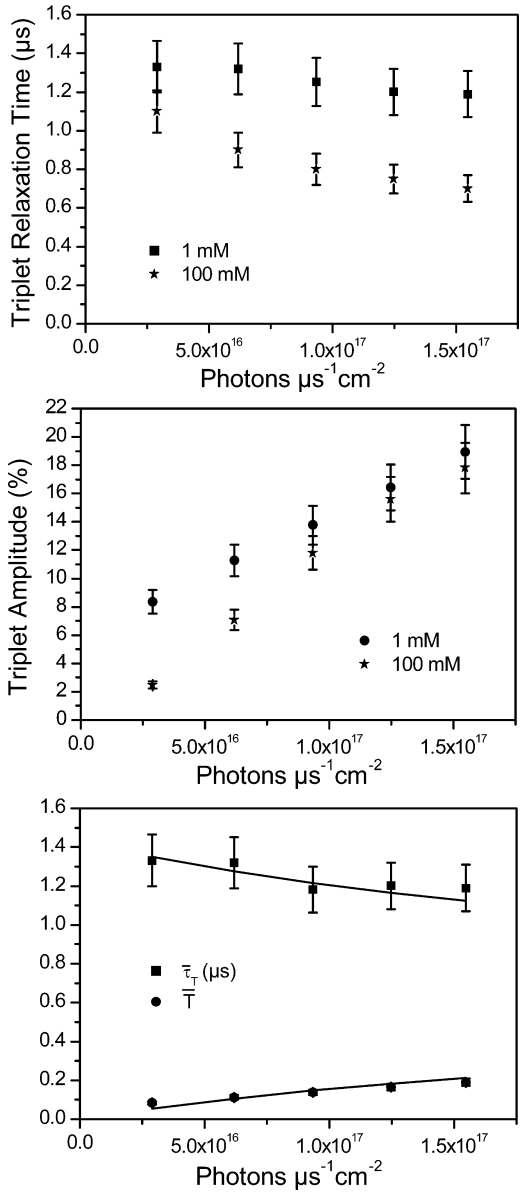

Figure 7. Comparison of measured triplet-state parameters for Rh6G in water at two different ionic strengths (1 and 100 mM). Error bars show estimated errors of ±10%. The upper graph shows $\bar{\tau}_t$ at 1 mM (filled squares) and 100 mM (filled stars). The middle graph shows $\bar{T}$ at 1 mM (filled circles) and 100 mM (filled stars). The lower graph shows the corresponding weighted and spatially averaged global fits of the TIR-FCS data for Rh6G at 1 mM ionic strength, $k_{ISC} = 2.1 \pm 0.2\ \mu s^{-1}$ and $k_T = 0.70 \pm 0.05\ \mu s^{-1}$, with $\bar{\tau}_t$ (filled squares) and $\bar{T}$ (filled circles). The concentration of Rh6G was 50 nM.

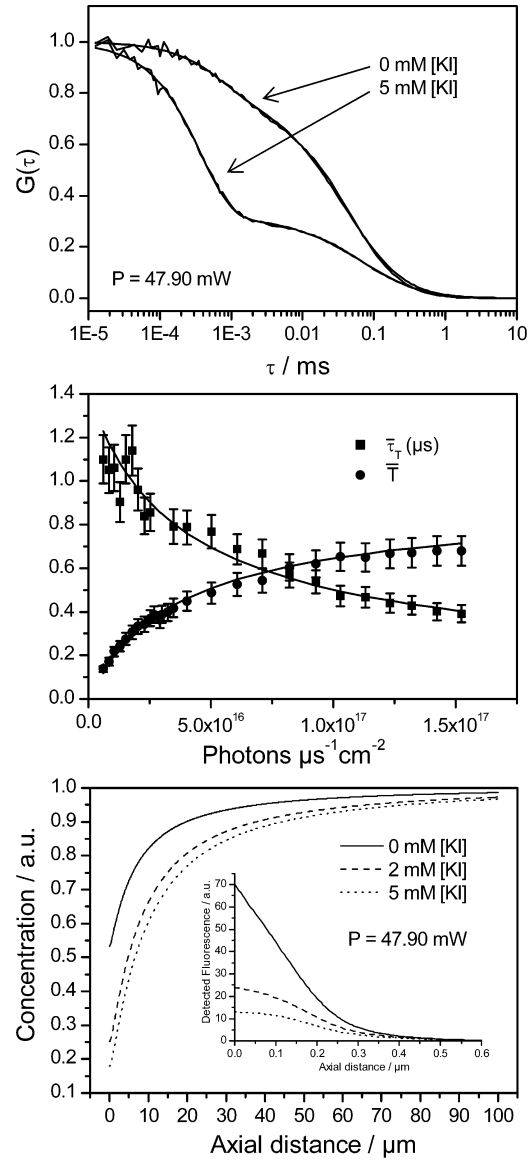

Figure 8. Top: Normalized correlation curves of Rh6G in PBS buffer without and with addition of 5 mM potassium iodide, KI, and the corresponding TIR-FCS fits to eq 6 at maximum laser excitation power. Middle: Resulting curves of measured triplet-state parameters with 5 mM potassium iodide, $\bar{\tau}_t$ (filled squares) and $\bar{T}$(filled circles), and the corresponding weighted and spatially averaged global fits, $k_{ISC} = 24.4 \pm 1.5\ \mu s^{-1}$ and $k_T = 0.71 \pm 0.04\ \mu s^{-1}$. Error bars show estimated errors of ±10%. The concentration of Rh6G was 50 nM. Bottom: Computer simulations of how the concentration of Rh6G molecules changes in the axial direction without and with addition of potassium iodide (2 and 5 mM) at maximum laser excitation power. The inset shows the axially detected fluorescence profiles in the observation volume. Note the large fluorescence saturation effects in the vicinity of the interface with high potassium iodide concentrations.

deduced for the 5 mM solution: $k_{ISC} = 24.4 \pm 1.5\ \mu s^{-1}$ and $k_T = 0.71 \pm 0.04\ \mu s^{-1}$. Table 2 summarizes all measured potassium iodide concentrations and the deduced TIR-FCS rates. It also contains the measured fluorescence decay rates, τ_f^{-1}, and a comparison with previously deduced triplet rates in bulk solution obtained by confocal FCS.

Discussion

An interaction-free interface is an important prerequisite for studying triplet-state kinetics using TIR-FCS and thereby learning more about the photophysics of fluorescent dyes near glass surfaces. No interactions that physically or chemically alter the properties of the dye under investigation should occur with the interface. If this is not the case, then either the new surface-generated properties might be worthy of a study on their own, or it is necessary to minimize the interaction by altering the properties and microenvironment of the surface. In this study, we find that uncleaned cover glasses cannot be used because they show very strong binding and sticking for all the investigated dyes. After extensive ultrasonic cleaning and plasma etching of the cover glasses, binding only at rare spots is occasionally visible on the CCD and in the correlation curves. To avoid influences from the so-called hot spots, which have been shown to be topological variations enhancing binding,[87] all TIR-FCS measurements are done on areas lacking such spots.

The charged homogeneous surface can still show interactions with negatively and positively charged fluorescent dyes (fluorescein, dianionic; ATTO 488, anionic; rhodamine 110, zwitterionic/neutral; rhodamine 123 and rhodamine 6G, cationic). This can be seen as a decrease or increase in the diffusion time due to repulsion or attraction with the charged surface.[88,89] To minimize and shield any electrostatic effects, sodium chloride is added to the dye solutions. A salt concentration of 100−150 mM is used, which generates an effectively neutral surface as the sodium ions are attracted to, and shield, the unpaired negative silanol groups at the silica interface. The Debye length, i.e., the electrostatic field's decay length (1/*e* value), is under these conditions less than 1 nm, but is sufficient to effectively minimize any electrostatic dye−surface interactions.[90] Here we have considered glass interfaces, but other dielectric materials (e.g., mica or even fused silica) or chemically modified surfaces (e.g., silanized) could also have been investigated. However, this falls outside the scope of this work.

To ensure that all investigations are done under the same optical conditions, the TIR-FCS setup is calibrated with fluorescein and rhodamine 123 at fixed power and fixed angle of incidence, before the triplet-state measurements are conducted. If the calibration were to not deliver the same optimal diffusion time, counts per molecule, and tripletstate parameters as previously, the laser beam path would be readjusted (by realigning the in-coupling mirrors and focusing lens). If a value for the diffusion coefficient, D, is assumed, the calibration measurements may also be used to estimate the axial extent of the observation volume, h, which is approximately equal to the penetration depth of the evanescent field, d.[57,91] Autocorrelation curves are thereafter analyzed at different excitation irradiances, and the rates governing the triplet state are determined for all fluorescent dyes.

To avoid the possibility of influence from the protonation dynamics of fluorescein, i.e., $H_2Fl \leftrightarrow HFl^-$ ($pK_a = 4.4$) and $HFl^- \leftrightarrow Fl^{2-}$ ($pK_a = 6.4$),[92] which could disturb the correlation analysis due to overlapping time ranges of fluorescence fluctuations, a Tris buffer with pH 8.2 is used. This ensures that fluorescein remains in its dianionic form. The resulting TIR-FCS k_{ISC} rate and k_T rates for fluorescein shown in Figure 3 are higher than the reference rates determined by confocal FCS. The same trend of higher triplet rates at the dielectric surface is also seen for ATTO 488, rhodamine 110, and rhodamine 123, all investigated at physiological conditions using PBS buffer with pH 7.4.

A reason for the higher rates at the surface could be an underestimate of the axial extent of the excitation, i.e., d. This is usually not the case due to scattering from surface pits in the glass slide, which results in additional light in the evanescent zone, equivalent to a slightly higher value of d.[94] Also an underestimate of the magnitude of the evanescent field would lead to an overestimation of the rates. To determine the field magnitude, the angle of incidence is measured with respect to the critical angle, θ_c, and thus, the values of the linear translator holding the focusing lens and dichroic mirror are calibrated to the angle of incidence (cf. Figure 1). The maximum occurs when total internal reflection of the laser beam is first seen in the microscope. We estimate that this calibration procedure generates at most a 0.2° error in the angle of incidence, which transforms into a less than 5% error in the field magnitude (i.e., η in eq 3). Circular polarization is achieved by adjusting the $\lambda/4$ wave plate so that the laser power after the dichroic mirror and an additional linear polarizer remains constant as the polarizer is rotated. The estimate of the lateral extent of the TIR excitation (i.e., R in eq 7) also contributes to an uncertainty in the intensity distribution. The lateral extent is deduced from the detected image of fluorescence from the surface of the glass coverslip, by fitting it to a Gaussian in the x and y directions and averaging the two radii (cf. the inset in Figure 1).

In addition, the values used for the excitation intensity distribution also depend on the saturation properties of the dye. In confocal FCS, high laser powers often generate distortion of the emission profile,[93] which may lead to underestimation of the k_{ISC} rates.[47] Furthermore, a high excitation irradiance opens up additional relaxation channels, e.g., reverse intersystem crossing that may lower the k_T rates.[27,28] The confocal reference rates might therefore be slightly underestimated. The relatively low irradiances used in TIR-FCS do not introduce the problems just mentioned. However, the fluorescence lifetime,τ_f, used in calculating the triplet rates should possibly be modified slightly. The reason for this is that the interface may modify the electromagnetic decay channels of the fluorophore.[95] For a bare dielectric surface this can lead to a decrease in fluorescence lifetime by 5−10% compared to that in bulk solution.[78] To take this into account, the determined rates for k_{ISC} of fluorescein, ATTO 488, rhodamine 110, and rhodamine 123 should be increased about 5−10%. Pulsed laser excitation and TCSPC analysis would allow measurement of the surface-modified fluorescence emission rates directly in the TIR-FCS setup. Enhancement of the k_T rates in the vicinity of the dielectric surface might also be explained by the effect of the changed electromagnetic mode density at interfaces.[50] However, the decay of the triplet state is highly nonradiative in aerated solutions at room temperature, meaning that only a very small radiative fraction is contributing to the shorter triplet relaxation rates. Literature values for comparison of the triplet-state kinetic rates at a dielectric interface for fluorescein, ATTO 488, rhodamine 110, and rhodamine 123 dyes are difficult to find. Often other dyes are studied, in addition to differences in theoretical assumptions and experimental conditions.[49,50]

From the discussion above it is seen that the triplet rates are similar although slightly higher at a glass surface than in the bulk solution. This is also true for rhodamine 6G, but the differences between the rates for TIR-FCS and confocal FCS are significantly higher. Additionally, the triplet amplitudes and the triplet relaxation times show a strong dependence on the dye concentration (cf. Figure 6). For all other studied dyes, no changes in triplet relaxation times and triplet amplitudes are seen when the concentrations are changed. The reason for this behavior is most probably due to the hydrophobicity of Rh6G,[96–98] which introduces interactions with the interface, which in the end may open up new efficient fluorophore relaxation channels.[96,99–101] In the case of Rh6G, formation of dye aggregates is often accompanied by a change in the radiative and radiationless transition probabilities.[97] Furthermore, aggregates in the form of adsorbed monomers, dimers, and trimers have been shown to play an important role in long-range energy- and electron-transfer mechanisms for freely diffusing Rh6G molecules.[99] The strong spin−orbital coupling induced by aggregates through spreading in their singlet energy levels can actually increase intersystem crossing rates.[96] Shortening of triplet relaxation times, via triplet−triplet and triplet−singlet annihilations, may additionally be enhanced by surface-adsorbed aggregates.[98]

The exact nature of the Rh6G surface interactions and the complex kinetics is beyond the scope of this paper. To be able to study, for example, the photophysics of free fluorophore and surface-bound aggregates, one actually needs to modify eq 6.

In its simplest form, two triplet-state populations, $\bar{T}$, and two triplet decay times, $\bar{\tau}_t$, can be introduced. Due to overlapping time scales it is not usually possible to resolve two (or more) photophysical components in the correlation curve. However, what might be seen though is a combination of the two relaxation times, or more specifically the decay constant of the autocorrelation function shows the reciprocal of the sum of the two rates. Note that if any of these rates is significantly larger than the other, it will dominate the decay of $G(\tau)$. Figure 5 clearly shows that effect when one triplet relaxation process dominates the correlation function. The very fast $\bar{\tau}_t$ values are assumed to occur due to aggregate-mediated quenching.

The triplet amplitude of $G(\tau)$ also contains information about free and bound species. Here, each contribution is weighted by the fluorescence brightness squared. Because of uncertainties in the emission probabilities of the adsorbed dyes, it will however be difficult to accurately weight the triplet amplitudes. For example, aggregation studies show the existence of fluorescent and nonfluorescent aggregates of Rh6G. Nonfluorescent species seem to prevail in polar solvents such as water, whereas fluorescent aggregates are seen in weakly polar solvents or in the adsorbed state.[97] Furthermore, the acidity and the hydrophobicity of the surface also influence the state of aggregation and the photophysical properties of the adsorbed species.[101,102] The actual TIR-FCS measurement shows both lower and higher triplet amplitude compared to confocal reference values (cf. Figure 5). This indicates that the correlation model used to fit the initial data probably needs modifications, which incorporate additional species and photophysical terms.

To minimize the amount of adsorbed Rh6G molecules, lower dye concentrations were investigated. Adsorption of rhodamine 6G has been studied extensively with TIR-FCS, and it has been noticed that a large energy binding term is needed to explain Rh6G's aggressive adsorption on glass surfaces.[61,62] It has also been recognized that adsorbed molecules may experience a less polar and a more hydrophobic microenvironment at a surface.[102] The interface-specific behavior of Rh6G might then be understood by looking at its structure, which contains long hydrophobic carbon chains attached to the fluorescent aromatic structure. The long carbon chains will bind strongly to silica surfaces having hydrophobic environments. This will be followed by a possible stacking of the aromatic units, which leads to an increased probability of generating aggregates that in the end may influence the triplet parameters. In comparison of low- and high-concentration Rh6G solutions (1 nM vs 50 nM), larger $\bar{\tau}_t$ and $\bar{T}$ values are shown in the former case, indicating a decreased influence from surface-adsorbed species. However, even the low Rh6G concentration generates higher intersystem crossing and triplet decay rates compared to confocal FCS. The larger k_{ISC} is probably explained by influences from the remaining aggregates, which through an increased spin−orbital coupling enhance intersystem crossing.[96] The smaller enhancement seen in k_T might in part be explained by remaining aggregate-mediated quenching, but also by the effect of the changed electromagnetic mode density at the surface.[50] This is in sharp contrast to bulk solution studies where no influences from aggregation on the triplet parameters are seen below 100 μM.[14]

Strong aggregation dependence has also been observed in the case of rhodamine 6G when chloride was acting as the counteranion.[97] The predicted trends of increased $\bar{\tau}_t$ and $\bar{T}$ values due to less aggregation are visible in Figure 7 when the ionic strength is lowered. This time though, less interacting aggregates are entangled with a change in the electrostatic potential. The electrostatic potential attracts positively charged Rh6G dyes closer and harder to the surface, forcing them to experience higher excitation intensities for longer times. Because of this effect, the changes seen in the triplet relaxation times and triplet amplitudes with changed excitation irradiance are slightly biased. The largest bias is seen at low intensities in Figure 7 where $\bar{\tau}_t$ increases less and $\bar{T}$ increases more than what would have been seen without the attraction. Smaller biases occur at high excitation intensities where attracted molecules may be bleached effectively.

Furthermore, low salt concentration not only influences aggregation and electrostatic interactions, but may also affect the distribution of Rh6G species present at the surface. The cationic dye form $Rh6G^+$ and the contact ion pair $Rh6G^+:Cl^-$ may both be present in solutions containing sodium chloride. It has been shown that the cationic form is dominant in aqueous solutions, but that there is a shift toward increased amounts of ion pairs at interfaces.[102] The cationic form and the ion pair may in addition have shifted emission spectra and different fluorescence quantum yields.[103] Assuming a higher quantum yield for $Rh6G^+:Cl^-$ could possibly explain the very small increase of $\bar{T}$ seen in Figure 7. At lower chloride concentrations the amount of ion pairs at the interface decreases. This would result in a decreased fluorescence brightness that lowers the weighting factor of the triplet amplitude. Our TIR-FCS analysis alone does not reveal enough details of this complex surface chemistry of Rh6G.[104] Targeting the photophysics of different Rh6G species and possible aggregates is left for future investigations.

Another dye−solvent effect that is of interest is the well-known property of fluorescence quenching by potassium iodide.[86] The quenching is a result of either stationary or collision-induced spin−orbital perturbations.[105] In the first case a strong stationary complex may be formed, whereas in the latter case diffusion-controlled collisions take place.[106] Under the influence of the perturbing action of potassium iodide the triplet-state rate parameters of Rh6G are greatly changed, as has already been shown with confocal FCS.[14,47] The same effects are shown in Figure 8 with TIR-FCS by addition of 5 mM iodide, giving rise to large triplet populations and fast triplet relaxation times, which transform into increased measured triplet rates. In contrast to the bulk solution case the extracted k_{ISC} and k_T rates do not show a linear dependence over the whole concentration range. The trend of getting similar rates with TIR-FCS and confocal FCS decreases as the iodide concentration is lowered. We attribute this to influences from dye aggregates that enhance the triplet rates (cf. Figure 5) and to changes in the saturation and bleaching properties of Rh6G at the surface.

In this study we have generally assumed that all Rh6G fluorophores are photochemically intact; i.e., no photobleaching may occur. The saturation and photobleaching properties of the fluorophore under investigation can differ considerably with different environmental parameters.[19–21] The ratio of the intersystem crossing rate and the triplet relaxation rate actually gives an estimate of how prone the dye is to photobleaching. Addition of potassium iodide greatly increases this ratio, which leads to increased photodestruction probabilities. Computer simulations of how the concentration of Rh6G molecules in the sample volume is depleted in the presence of bleaching are shown in Figure 8. A strong depletion of molecules within the observation volume and its surroundings is predicted. In the vicinity of the surface, high triplet-state buildup of Rh6G due to very high excitation irradiances is further increased upon addition of potassium iodide. This inevitably leads to promoted photode-

struction of fluorophores at the interface, which makes the overall concentration depletion even larger. The inset in Figure 8 shows the saturation of detected fluorescence in the observation volume when potassium iodide is added. When all of these effects are taken into account, there is a resulting reduction in the relative fluorescence contributions from Rh6G molecules close to the surface compared to those further away. This leads to a bias in the correlation analysis toward noninterfacial Rh6G molecules, which may explain the similar triplet rates seen with TIR-FCS and confocal FCS at high potassium iodide concentrations (cf. Table 2).

A comparison of the triplet-state kinetic rates of Rh6G with values reported in the literature is somewhat difficult to make. As shown previously, the data for Rh6G can vary by more than an order of magnitude in bulk solution.[107] However, our FCS reference values are well supported in the literature.[108] The determined triplet rates may differ considerably due to differences in how well the excitation intensity distribution is approximated. The most common assumption applied is a homogeneous intensity distribution (uniform profile), which is assumed valid in confocal FCS when small pinholes or expanded focal volumes are used.[46,49] Even within this approximation differences do occur, especially concerning choosing the peak value, I_0, of the uniform profile. The choice of a lower effective peak intensity value, $I_0/2$, may account for the saturation of fluorescence that occurs at large excitation intensities.[27,93] Differences in the solvents also influence the k_{ISC} and k_T rates by means of the relatively high environmental sensitivity of the triplet state.[47] Changing the physical surroundings of the fluorophore, such as embedding it in a polymer or placing it on a metallic interface, may also change the triplet-state kinetics.[42,50] The work by Jerome and co-workers[51] is an investigation that somewhat resembles our triplet-state TIR-FCS studies at dielectric interfaces. Their study investigates the photokinetics of rhodamine 6G dissolved in a water−glycerol mixture in which the dye molecules diffuse in nanometric aluminum apertures placed on top of a standard microscope coverslip. To derive the triplet-state kinetic parameters by FCS, the authors assumed the excitation distribution to be uniform within the aperture. Compared to solution reference measurements, large enhancements in the intersystem crossing and triplet relaxation rates were seen. Our study indicates that similar larger k_{ISC} and k_T rates can be observed for Rh6G with TIR-FCS on plain dielectric surfaces. Another interesting finding is that one may see deviation resembling our assumed aggregation-induced effects also in the nanometric apertures, i.e., both higher and lower $\bar{T}$ values, which generate deviations in fits to deduce the triplet rates (cf. Figure 5 in this study and Figure 3B in ref 51).

Conclusions

We have studied the triplet-state kinetic rates of several fluorescent dyes at dielectric interfaces with TIR-FCS. As the triplet state is responsible for the saturation of the fluorescence emission and for the finite photodegradation lifetime of the fluorescent dyes, it is important to investigate its kinetics at interfaces. This allows a better understanding of the fundamental photophysical processes and the possibility to find optimized conditions for ultrasensitive fluorescence microscopy. The steady-state triplet relaxation time, $\bar{\tau}_t$, and triplet amplitude, $\bar{T}$, are determined by applying correlation analysis at different excitation irradiances. To rigorously deduce the triplet rates, i.e., the intersystem crossing rate, k_{ISC}, and the triplet relaxation rates, k_T, from the triplet relaxation time and triplet amplitude, the latter are weighted by the detected fluorescence from the observation volume.[47] To derive a correct estimate of the detected fluorescence from the dielectric interface in TIR-FCS, the specific properties of evanescent excitation and anisotropic emission are considered and incorporated into the triplet rate analysis. For all investigated dyes, slightly higher k_{ISC} and k_T rates are seen at the surface compared to solution measurements. This enhancement we attribute to possible modifications of photophysical properties occurring at dielectric interfaces.[50,78,95] Our results additionally show in the case of rhodamine 6G the existence of specific interface-induced effects, generating significantly higher triplet rates. These effects are probably due to influences from dye−dye, dye−solvent, and dye−surface interactions, as indicated through measurements with changes in dye concentration and ionic strength. This shows that analysis of triplet-state kinetics by TIR-FCS not only results in a better understanding of the interfacial photophysical properties of the dyes, but also provides a means for probing the microenvironment near dielectric interfaces.

Acknowledgment. The European Community (Spotlite-project), the Swedish Foundation for Strategic Research (Bio-X), and the Swedish Research Council (Grant VR-621-2006-3197) are acknowledged for financial support of this project. Personal scholarships awarded by the Wenner-Gren Foundation to K.H. and by Leif Jonsson's Minnesfond to H.B. are also acknowledged. Finally, Tor Sandén is acknowledged for stimulating discussions.

Appendix

Given the three-state model of Figure 9, the occupation probabilities S_0, S_1, and T of the corresponding electronic states of a fluorophore, located at a point $\mathbf{r}$ at a time t, can be derived from the following equation system:[47]

$$\frac{d}{dt}\begin{pmatrix} S_0(\mathbf{r},t) \\ S_1(\mathbf{r},t) \\ T(\mathbf{r},t) \end{pmatrix} = \begin{bmatrix} -k_{01}(\mathbf{r}) & k_{10} & k_T \\ k_{01}(\mathbf{r}) & -(k_{ISC}+k_{10}) & 0 \\ 0 & k_{ISC} & -k_T \end{bmatrix} \begin{pmatrix} S_0(\mathbf{r},t) \\ S_1(\mathbf{r},t) \\ T(\mathbf{r},t) \end{pmatrix}$$

The initial condition where the fluorophore is in its ground singlet state at $t = 0$ can be formulated as

$$\begin{pmatrix} S_0(\mathbf{r},0) \\ S_1(\mathbf{r},0) \\ T(\mathbf{r},0) \end{pmatrix} = \begin{pmatrix} 1 \\ 0 \\ 0 \end{pmatrix}$$

This initial condition applies to the situation that follows upon a fluorescence photon emission at time $t = 0$. It also applies to a fluorophore that has not been subject to excitation for a long enough time before $t = 0$, such that full relaxation from S_1, or from T_1, back to S_0 has taken place. The decay of the singlet state by fluorescence or internal conversion is furthermore assumed to be much faster than either of the processes of intersystem crossing or decay of the triplet state, i.e., $k_{10} \gg k_{ISC}$, k_T. With application of the last assumption and the initial condition, the following occupation probabilities are deduced for a fluorescent molecule located at $\mathbf{r}$ that is subject to a stationary excitation irradiance $I(\mathbf{r})$ starting at $t = 0$:

$$S_0(\mathbf{r},t) = \frac{k_{10}k_T}{k_{01}(\mathbf{r})(k_{ISC}+k_T)+k_{10}k_T} e^{\lambda_1(\mathbf{r})t} + \frac{k_{01}(\mathbf{r})}{k_{01}(\mathbf{r})+k_{10}} e^{\lambda_2(\mathbf{r})t} + \frac{k_{01}(\mathbf{r})k_{10}k_{ISC}}{(k_{01}(\mathbf{r})+k_{10})[k_{01}(\mathbf{r})(k_{ISC}+k_T)+k_{10}k_T]} e^{\lambda_3(\mathbf{r})t} \quad (1A)$$

$$S_1(\mathbf{r},t) = \frac{k_{01}(\mathbf{r})k_T}{k_{01}(\mathbf{r})(k_{ISC}+k_T)+k_{10}k_T}e^{\lambda_1(\mathbf{r})t} - \frac{k_{01}(\mathbf{r})}{k_{01}(\mathbf{r})+k_{10}}e^{\lambda_2(\mathbf{r})t} + \frac{{k_{01}}^2(\mathbf{r})k_{ISC}}{(k_{01}(\mathbf{r})+k_{10})[k_{01}(\mathbf{r})(k_{ISC}+k_T)+k_{10}k_T]}e^{\lambda_3(\mathbf{r})t} \quad (2A)$$

$$T(\mathbf{r},t) = \frac{k_{01}(\mathbf{r})k_{ISC}}{k_{01}(\mathbf{r})(k_{ISC}+k_T)+k_{10}k_T}e^{\lambda_1(\mathbf{r})t} - \frac{k_{01}(\mathbf{r})k_{ISC}}{k_{01}(\mathbf{r})(k_{ISC}+k_T)+k_{10}k_T}e^{\lambda_3(\mathbf{r})t} \quad (3A)$$

where $k_{01}(\mathbf{r}) = \sigma I(\mathbf{r})$ and σ is the absorption cross section. The eigenvalues λ_1, λ_2, and λ_3 in eqs 1A−3A are related to the relaxation modes of the population kinetics of the three states and given by

$$\lambda_1(\mathbf{r}) = 0 \quad (4A)$$

$$\lambda_2(\mathbf{r}) = -(k_{01}(\mathbf{r})+k_{10}) \quad (5A)$$

$$\lambda_3(\mathbf{r}) = -\left(k_T + \frac{k_{01}(\mathbf{r})k_{ISC}}{k_{01}(\mathbf{r})+k_{10}}\right) \quad (6A)$$

The first eigenvalue, λ_1, is zero, indicating that the populations in the three states will approach a steady state as $t \rightarrow \infty$. This follows from the fact that the three-state model of Figure 9 constitutes a closed system, assuming a constant total probability of 1 and no photobleaching. The second eigenvalue, λ_2, is of high magnitude and represents the so-called antibunching term. It is related to the time it takes until the population of the two singlet states have equilibrated with respect to each other, following onset of excitation at $t = 0$. The magnitude of the third eigenvalue, λ_3, is related to the rate at which the buildup of the triplet-state population takes place. Its inverse is referred to as the triplet relaxation time τ_T.

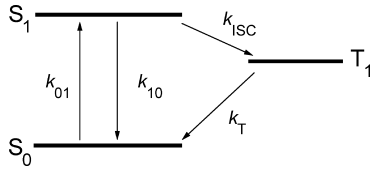

Figure 9. Three-state electronic model, including the singlet ground state S_0, the first excited singlet state S_1, and the lowest triplet state T_1. Here, k_{01}, k_{10}, k_{ISC}, and k_T are the rate constants for excitation from S_0 to S_1, relaxation of S_1 to S_0, intersystem crossing from S_1 to T_1, and relaxation of T_1 to S_0, respectively.

References and Notes

(1) D Leake, M. C.; Chandler, J. H.; Wadhams, G. H.; Bai1, F.; Berry, R. M.; Armitage, J. P. *Nature (London)* **2006**, *443*, 355.
(2) Elf, J.; Li, G.-W.; Xie, X. S. *Science* **2007**, *316*, 1191.
(3) Hell, S. W. *Science* **2007**, *316*, 1153.
(4) Westphal, V.; Rizzoli, S. O.; Lauterbach, M. A.; Kamin, D.; Jahn, R.; Hell, S. W. *Science* **2008**, *320*, 246.
(5) Weber, J. *Opt. Commun.* **1973**, *7*, 420.
(6) Widengren, J.; Rigler, R. *Bioimaging* **1996**, *4*, 149.
(7) Eggeling, C.; Widengren, J.; Rigler, R.; Seidel, C. A. M. *Anal. Chem.* **1998**, *70*, 2651.
(8) Eggeling, C.; Widengren, J.; Rigler, R.; Seidel, C. A. M. In *Applied Fluorescence in Chemistry, Biology and Medicine*; Rettig, W., Strehmel, B., Schrader, S., Seifert, H. Eds.; Springer-Verlag: Berlin, 1999.
(9) Song, L.; Varma, C. A. G. O.; Verhoeven, J. W.; Tanke, H. J. *Biophys. J.* **1996**, *70*, 2959.
(10) Zondervan, R.; Kulzer, F.; Kol'chenko, M. A.; Orrit, M. *J. Phys. Chem. A* **2004**, *108*, 1657.
(11) Tsien, R. Y.; Ernst, L.; Waggoner, A. In *Handbook of Confocal Microscopy*, 3rd ed.; Pawley, J. B. Ed.; SpringerScience + Business Media: New York, 2006.
(12) Donnert, G.; Keller, J.; Medda, R.; Andrei, M. A.; Rizzoli, S. O.; Lührmann, R.; Jahn, R.; Eggeling, C.; Hell, S. W. *Proc. Natl. Acad. Sci. U.S.A.* **2006**, *103*, 1440.
(13) Donnert, G.; Eggeling, C.; Hell, S. W. *Nat. Methods* **2007**, *4*, 81.
(14) Sandén, T.; Persson, G.; Thyberg, P.; Blom, H.; Widengren, J. *Anal. Chem.* **2007**, *79*, 3330.
(15) Person, G.; Thyberg, P.; Widengren, J. *Biophys. J.* **2008**, *94*, 977.
(16) Jacques, V.; Murray, J. D.; Marquier, F.; Chauvat, D.; Grosshans, F.; Treussart, F. *Appl. Phys. Lett.* **2008**, *93*, 203307.
(17) Satsoura, D.; Leber, B.; Andrews, D. W.; Fradin, C. *ChemPhysChem* **2007**, *8*, 834.
(18) Hoebe, R. A.; van Oven, C. H.; Gadella, T. W. J., Jr.; Dhonukshe, P. B.; van Noorden, C. J. F.; Manders, E. M. M. *Nat. Biotechnol.* **2007**, *25*, 249.
(19) Rasnik, I.; McKinney, S. A.; Ha, T. *Nat. Methods* **2006**, *3*, 891.
(20) Widengren, J.; Chmyrov, A.; Eggeling, C.; Löfdahl, P-Å.; Seidel, C. A. M. *J. Phys. Chem. A* **2007**, *111*, 429.
(21) Vogelsang, J.; Kasper, R.; Steinhauer, C.; Person, B.; Heilemann, M.; Sauer, M.; Tinnefeld, P. *Angew. Chem., Int. Ed.* **2008**, *47*, 5465.
(22) Echeverría Aitken, C.; Marshall, R. A.; Puglisi, J. D. *Biophys. J.* **2008**, *94*, 1826.
(23) Tian, H.; Yang, S. *J. Photochem. Photobiol., C* **2002**, *3*, 67.
(24) Weston, K. D.; Carson, P. J.; DeAro, J. A.; Buratto, S. K. *Chem. Phys. Lett.* **1999**, *308*, 58.
(25) English, D. S.; Furune, A.; Barbara, P. F. *Chem. Phys. Lett.* **2000**, *324*, 15.
(26) Hübner, Ch. G.; Renn, A.; Renge, I.; Wild, U. P. *J. Chem. Phys.* **2001**, *115*, 21.
(27) Widengren, J.; Seidel, C. A. M. *Phys. Chem. Chem. Phys.* **2000**, *2*, 3435.
(28) Ringemann, C.; Schönle, A.; Giske, A.; von Middendorff, C.; Hell, S. W.; Eggling, C. *ChemPhysChem* **2008**, *9*, 612.
(29) Hell, S. W.; Kroug, M. *Appl. Phys. B: Lasers Opt.* **1995**, *60*, 495.
(30) Bretschneider, S.; Eggeling, C.; Hell, S. W. *Phys. Rev. Lett.* **2007**, *98*, 218103.
(31) Fölling, J.; Bossi, M.; Bock, H.; Medda, R.; Wurm, C. A.; Hein, B.; Jakobs, S.; Eggeling, C.; Hell, S. W. *Nat. Methods* **2008**, *5*, 943.
(32) Enderlein, J. *Appl. Phys. Lett.* **2005**, *87*, 094105.
(33) Sandén, T.; Persson, G.; Widengren, J. *Anal. Chem.* **2008**, *80*, 9589.
(34) Lewis, G. N.; Kasha, M. *J. Am. Chem. Soc.* **1944**, *66*, 2100.
(35) McClure, D. S. *J. Chem. Phys.* **1949**, *17*, 905.
(36) Kasche, V.; Lindqvist, L. *J. Phys. Chem.* **1964**, *68*, 817.
(37) Korobov, V. E.; Shubin, V. V.; Chibisov, A. K. *Chem. Phys. Lett.* **1977**, *45*, 498.
(38) *Dye Laser*, 3rd ed.; Schäfer, F. P. Ed.; Springer-Verlag: Berlin, 1990.
(39) *Single-Molecule Optical Detection; Imaging and Spectroscopy*; Basche, T., Moerner, W. E., Orrit, M., Wild, U. P. Eds.; VCH: Weinheim, Germany, 1999.
(40) *Single Molecule Detection in Solution—Methods and Applications*; Zander, Ch., Enderlein, J., Keller, R. A. Eds.; Wiley-VCH: Berlin, 2002.
(41) *Single Molecule Techniques: A Laboratory Manual*; Selvin, P. R., Ha, T. Eds.; Cold Spring Harbor Laboratory Press: Cold Spring Harbor, NY, 2008.
(42) Fleury, L.; Segura, J.-M.; Zumofen, G.; Hecht, B.; Wild, U. P. *Phys. Rev. Lett.* **2000**, *84*, 1148.
(43) Zondervan, R.; Kulzer, F.; Orlinskii, S. B.; Orrit, M. *J. Phys. Chem. A* **2003**, *107*, 6770.
(44) Schuster, J.; Cichos, F.; von Borczykowski, C. *Appl. Phys. Lett.* **2005**, *87*, 1915.
(45) Clifford, J. N.; Bell, T. D. M.; Tinnefeld, P.; Heilemann, M.; Melnikov, S. M.; Hotta, J.-I.; Sliwa, M.; Dedecker, P.; Sauer, M.; Hofkens, J.; Yeow, E. K. L. *J. Phys. Chem. B* **2007**, *111*, 6987.
(46) Widengren, J.; Rigler, R.; Mets, Ü. *J. Fluoresc.* **1994**, *4*, 255.
(47) Widengren, J.; Mets, Ü.; Rigler, R. *J. Phys. Chem.* **1995**, *99*, 13368.
(48) Heupel, Ma.; Gregor, I.; Becker, St.; Thiel, E. *Int. J. Photoenergy* **1999**, *1*, 1.
(49) Yeow, E. K. L.; Melnikov, S. M.; Bell, T. D. M.; de Schryver, F. C.; Hofkens, J. *J. Phys. Chem A* **2006**, *110*, 1726.
(50) Stefani, F. D.; Krasimir, V.; Bocchio, N.; Gaul, F.; Pomozzi, A.; Kreiter, M. *New J. Phys.* **2007**, *9*, 21.
(51) Wenger, J.; Cluzel, B.; Dintinger, J.; Bonod, N.; Fehrembach, A.-L.; Popov, E.; Lenne, P.-F.; Ebbesen, T. W.; Rigneault, H. *J. Phys. Chem. C* **2007**, *111*, 11469.
(52) Magde, D.; Elson, E.; Webb, W. W. *Phys. Rev. Lett.* **1972**, *29*, 705.
(53) Rigler, R.; Mets, 951 > U.; Widengren, J.; Kask, P. *Eur. Biophys. J.* **1993**, *22*, 169.

(54) *Fluorescence Correlation Spectroscopy—Theory and Application*; Rigler, R., Elson, E. S. Eds.; Springer-Verlag: Berlin, 2001.
(55) Thompson, N. L.; Steele, B. L. *Nat. Protocol* **2007**, *2*, 878.
(56) Ruckstuhl, T.; Seeger, S. *Opt. Lett.* **2004**, *29*, 569.
(57) Hassler, K.; Anhut, T.; Rigler, R.; Gösch, M.; Lasser, T. *Biophys. J.* **2005**, *88*, L1.
(58) Burghardt, T. P.; Ajtai, K.; Borejdo, J. *Biochemistry* **2006**, *45*, 4058.
(59) Thompson, N. L.; Burghardt, T. P.; Axelrod, D. *Biophys. J.* **1981**, *33*, 435.
(60) Thompson, N. L.; Axelrod, D. *Biophys. J.* **1983**, *43*, 103.
(61) Hansen, R. L.; Harris, J. M. *Anal. Chem.* **1998**, *70*, 4247.
(62) Hansen, R. L.; Harris, J. M. *Anal. Chem.* **1998**, *70*, 2565.
(63) McCain, K. S.; Schluesche, P.; Harris, J. M. *Anal. Chem.* **2004**, *76*, 930.
(64) McCain, K. S.; Harris, J. M. *Anal. Chem.* **2003**, *75*, 3616.
(65) Lieto, A. M.; Cush, R. C.; Thompson, N. L. *Biophys. J.* **2003**, *85*, 3294.
(66) Starr, T. E.; Thompson, N. L. *J. Phys. Chem. B* **2002**, *106*, 2365.
(67) Pero, J. K.; Haas, E. M.; Thompson, N. L. *J. Phys. Chem. B* **2006**, *110*, 10910.
(68) Leutenegger, M.; Blom, H.; Widengren, J.; Eggeling, C.; Gösch, M.; Leitgeb, R. A.; Lasser, T. *J. Biomed. Opt.* **2006**, *11*, 040502.
(69) Hassler, K.; Rigler, P.; Blom, H.; Rigler, R.; Widengren, J.; Lasser, T. *Opt. Exp.* **2007**, *15*, 5366.
(70) Sonesson, A. W.; Blom, H.; Hassler, K.; Elofsson, U. M.; Callisen, T. H.; Widengren, J.; Brismar, H. *J. Colloid Interface Sci.* **2008**, *317*, 449.
(71) Ohsugi, Y.; Saito, K.; Tamura, M.; Kinjo, M. *Biophys. J.* **2006**, *91*, 3456.
(72) Ries, J.; Ruckstuhl, T.; Verdes, D.; Schwille, P. *Biophys. J.* **2008**, *94*, 221.
(73) Axelrod, D.; Burghardt, T. P.; Thompson, N. L. *Annu. Rev. Biophys. Bioeng.* **1984**, *13*, 247.
(74) Axelrod, D.; Hellen, E. H.; Fulbright, R. M. In *Topics in Fluorescence Spectroscopy, Vol. 3: Biological Applications*; Lakowicz, J. R. Ed.; Plenum Press: New York, 1992.
(75) Lukosz, W.; Kunz, R. E. *J. Opt. Soc. Am.* **1977**, *67*, 1607.
(76) Lukosz, W.; Kunz, R. E. *J. Opt. Soc. Am.* **1977**, *67*, 1615.
(77) Lukosz, W. *J. Opt. Soc. Am.* **1979**, *69*, 1495.
(78) Hellen, E. H.; Axelrod, D. *J. Opt. Soc. Am. B* **1987**, *4*, 337.
(79) Enderlein, J.; Ruckstuhl, T.; Seeger, S. *Appl. Opt.* **1999**, *38*, 724.
(80) Mertz, J. *J. Opt. Soc. Am. B* **2000**, *17*, 1906.
(81) Banerjee, A.; Kihm, K. D. *Phys Rev. E* **2005**, *72*, 042101.
(82) Ruckstuhl, T.; Enderlein, J.; Jung, S.; Seeger, S. *Anal. Chem.* **2000**, *72*, 2117.
(83) Hassler, K.; Leutenegger, M.; Rigler, P.; Rao, R.; Rigler, R.; Gösch, M.; Lasser, T. *Opt. Exp.* **2005**, *13*, 7415.
(84) Qian, H.; Elson, E. L. *Appl. Opt.* **1991**, *40*, 1185.
(85) *Advanced Time-Correlated Single Photon Counting Techniques*; Becker, W. Ed.; Springer-Verlag: Berlin, 2005.
(86) *Principles of Fluorescence Spectroscopy*; Lakowicz, J. R. Ed.; Springer Science: Singapore, 2006.
(87) Wirth, M. J.; Ludes, M. D.; Swinton, J. *Anal. Chem.* **1999**, *71*, 3911.
(88) Xu, X.-H.; Young, E. S. *Science* **1997**, *275*, 1106.
(89) Starr, T. E.; Thompson, N. L. *J. Phys. Chem. B* **2002**, *106*, 2365.
(90) *Electrolyte Solutions*; Robinson, R. A., Stoke, R. H. Eds.; Dover Publications: Mineola, NY, 2002.
(91) Harlepp, S.; Robert, J.; Darnton, N. C.; Chatenay, D. *Appl. Phys. Lett.* **2004**, *85*, 3917.
(92) Widengren, J.; Rigler, R. *J. Fluoresc.* **1997**, *7*, 211S.
(93) Davis, L.; Shen, G. *Curr. Pharm. Biotechnol.* **2006**, *7*, 287.
(94) Mattheyses, A. L.; Axelrod, D. J. *Biomed. Opt.* **2006**, *11*, 014006.
(95) Fort, E.; Grésillon, S. *J. Phys. D: Appl. Phys.* **2008**, *41*, 013001.
(96) McRae, E. G.; Kasha, M. *J. Phys. Chem.* **1958**, *28*, 721.
(97) Kemnitz, K.; Yoshihara, K. *J. Phys. Chem.* **1991**, *95*, 6095.
(98) Bryukhanov, V. V.; Ketsle, G. A.; Levshin, L. V. *J. Appl. Spectrosc.* **1978**, *28*, 507.
(99) López Arbeloa, F.; Ruiz Ojeda, P.; López Arbeloa, I. *J. Photochem. Photobiol., A* **1988**, *45*, 313.
(100) Ryl'kov, V. V.; Cheshev, E. A. *J. Appl. Spectrosc.* **1989**, *51*, 1317.
(101) Mialocq, J. C.; Hébert, Ph.; Armand, X.; Bonneau, R.; Morand, J. P. *J. Photochem. Photobiol., A* **1991**, *56*, 323.
(102) Zheng, X.-Y.; Wachi, M.; Harata, A.; Hatano, Y. *Spectrochim. Acta, Part A* **2004**, *60*, 1085.
(103) Köhn, F.; Hofkens, J.; De Schryver, F. D. *Chem. Phys. Lett.* **2000**, *321*, 372.
(104) López Arbeloa, F.; López Arbeloa, T.; Lage, G.; López Arbeloa, I.; De Schryver, F. C. *J. Photochem. Photobiol., A* **1991**, *56*, 313.
(105) Kasha, M. *J. Phys. Chem.* **1952**, *20*, 71.
(106) Ketsle, G. A.; Levshin, L. V.; Bryukhanov, V. V. *J. Appl. Spectrosc.* **1976**, *24*, 573.
(107) Asimov, M. M.; Gavrilenko, V. N.; Rubinov, A. N. *J. Luminesc.* **1990**, *46*, 243.
(108) Gregor, I.; Heupel, Ma.; Thiel, E. *Chem. Phys.* **2001**, *272*, 185.

JP8110088